

Influence of Dip and Velocity Heterogeneity on Reverse- and Normal-Faulting Rupture Dynamics and Near-Fault Ground Motions

by Daniel R. H. O'Connell*, Shuo Ma†, and Ralph J. Archuleta

Abstract We investigate the influence of fault dip (35° – 60°) and crustal velocity heterogeneity on rupture dynamics and near-fault ground motions from normal- and reverse-faulting. The same initial conditions were used, except for the direction of initial shear stress, in each dynamic rupture calculation. We used two 3D elastic finite-element approaches that employ split nodes for the computations. In homogeneous and weakly heterogeneous half-spaces with faults dipping $\lesssim 50^{\circ}$, maximum fault-normal peak velocities occurred on the hanging wall. However, for fault dips $\gtrsim 50^{\circ}$, maximum fault-normal peak velocities occurred on the footwall. Bilateral and unilateral rupture simulations in weakly heterogeneous media found that reverse-faulting slip velocities (frequency band 1–3.5 Hz) were on average 39% larger than those during normal faulting. However, on average reverse-faulting slip velocities were only 16% larger than normal-faulting slip velocities for frequencies < 1 Hz. This suggests that normal-faulting ground motions may have peak spectral accelerations at distinctly lower frequencies than reverse-faulting ground motions. Normal faults often juxtapose a low-velocity hanging-wall sedimentary basin against relatively stiff footwall rocks. A 3D velocity model was constructed with a thick (several kilometers) low-velocity basin with a strong shear-wave velocity contrast (factor of 3) across a fault dipping 55° . While the strong lateral velocity contrast reduced normal-faulting fault-normal peak velocities on the footwall, substantial (0.5–1 m/sec) fault-normal peak velocities remained on the footwall. Meanwhile even larger fault-normal peak velocities occurred on the more compliant hanging wall. These results indicate that simple amplitude parameterizations based on the hanging wall and/or footwall and the fault normal and/or fault parallel currently used in ground motion prediction relations may not be appropriate for some faults with dips $> 50^{\circ}$.

Introduction

There are relatively few near-fault strong ground motion recordings from $M > 6$ normal-faulting earthquakes and no recordings from $M > 6.7$ normal-faulting earthquakes (Spudich *et al.*, 1999; Ambraseys *et al.*, 2005). The 23 November 1980 Irpinia, Italy, earthquake, is the largest normal-faulting earthquake, at M 6.7 (Bernard and Zollo, 1989), that produced several near-fault strong motion recordings. Consequently, it is necessary to infer expected $M > 6.7$ near-fault normal-faulting strong motion behavior from dynamic simulations. These simulations can be validated by comparing simulated ground motion to the much more extensive near-fault strong motion database for reverse faulting. Oglesby

et al. (1998, 2000) simulated dynamic fault ruptures in a homogenous half-space to compare differences in fault slip velocities and free-surface peak velocities between normal- and reverse-faulting earthquakes as a function of dip. They found substantial differences in rupture behavior between normal- and reverse-faulting earthquakes even though they used identical initial conditions (except for the direction of applied initial shear stress). Their results were consistent with earlier thrust faulting results obtained from foam rubber faulting experiments (Brune, 1996) and a numerical lattice model (Shi *et al.*, 1998). Oglesby *et al.* (1998, 2000) did not explicitly consider the variations of hanging-wall and footwall peak fault-normal horizontal velocities and accelerations as a function of dip, nor did they compare and contrast the spectral shapes of radiated energy between normal and reverse faulting. In this article we use spontaneously propagating ruptures to investigate the influences of (1) fault dip and (2) weak and strong heterogeneity in crustal velocity

*Present address: William Lettis and Associates, Inc. Golden, Colorado 80401; oconnell@lettis.com.

†Present address: Department of Geophysics, Stanford University, Panama Mall 397, Stanford, California 94305.

on the dynamics of faulting and on the resulting ground motions.

We use two approaches to model a 3D spontaneous dynamic rupture. We use DYNELF (Andrews, 1999) for models in a uniform half-space. Details of the implementation of DYNELF are contained in Andrews (1999). DYNELF uses a time-weakening relation for the constitutive law for friction. The volume and fault are modeled with a finite-element split-node formulation along diagonal nodes with wedge elements to accommodate the dipping fault rupture. We use the 3D finite-element approach of Ma and Archuleta (2006) to evaluate the effects of crustal velocity heterogeneity on dynamic rupture and ground motions. This numerical method also uses a split-node formulation for the dynamics of faulting with wedge elements everywhere.

Investigations of Uniform Half-Space Dynamic Rupture and Ground Motions

The homogeneous half-space may be erroneously perceived as a simple problem. In fact, because of the complex character of free-surface scattering as a function of incidence angle (Aki and Richards, 1980, pp. 133–144 and 155–163), the free surface creates an intricate and complex problem for forensic investigations of the factors that control near-fault ground motions. The focus here is to extend the work of Oglesby *et al.* (1998, 2000) to investigate the fault-normal horizontal ground motion behavior as a function of the dip of the fault and style of dip-slip faulting (normal or reverse). We use nondimensional medium parameters to simplify the analyses for the case of a homogeneous half-space. Therefore, the shear-wave velocity and density are set to 1 km/sec and 1 g/cm³, respectively; the acoustic-wave velocity is 1.732 km/sec. This allows easy identification of various seismic phases in terms of their characteristic phase velocities. DYNELF uses time instead of distance to determine the interval over which friction decreases from yield friction to dynamic sliding friction. Longer values of time weakening would reduce seismic radiation (increased fracture energy), and smaller values of time weakening would increase seismic radiation (lower fracture energy). The important considerations are to use the same value of time weakening for all simulations so their results are directly comparable, to use a sufficiently large value to span several discrete timesteps to reduce numerical oscillations, but to keep the time weakening short enough to allow short-period seismic radiation. To meet these objectives the time weakening is set to 3 sec for all DYNELF calculations. Before presenting the DYNELF numerical calculations, it is important to identify the likely physical mechanisms that will influence rupture propagation and free-surface near-fault ground motions.

Rayleigh Pole

In an isotropic homogenous half-space, solutions of the secular Rayleigh-wave equation give the velocity of the

waves in the medium. The Rayleigh pole is the positive real root of the secular Rayleigh-wave equation and determines the conditions of Rayleigh surface-wave propagation. In a homogenous Poisson half-space, the Rayleigh wave propagates along the surface at a speed, c_R , that is 91.94% of the S -wave velocity. As the seismic source approaches the free surface, the Cagniard paths for free-surface ground-motion positions approach the Rayleigh pole on the real axis, and Rayleigh-wave amplitudes increase (Aki and Richards, 1980, pp. 223 and 234–243; Hudson, 1980, pp. 169–172). The Rayleigh-wave amplitude decreases in proportion to the depth of either the source or receiver. For a Poisson solid, free-surface Rayleigh-wave contributions from P waves become significant for incidence angles (relative to vertical) $\geq 27^\circ$ (Aki and Richards, 1980, p. 222), and S waves start producing strong Rayleigh-wave contributions for incident angles $\geq 78^\circ$ (Aki and Richards, 1980, p. 239). As fault dip decreases a greater proportion of a surface-rupturing fault's subsurface area becomes closer to the free surface, and the proportion of upgoing P and S waves with sufficiently large incident angles to induce significant Rayleigh-wave excitation near the fault increases, producing a stronger Rayleigh-wave field on the hanging wall farther from the surface trace of the fault than a fault with a steeper dip. Moreover, dips of 35° and 45° have a stronger Rayleigh-wave radiation pattern in the footwall direction than a fault dipping 60° (Johnson, 1974). Because the Rayleigh wave is nondispersive in an isotropic homogenous half-space, it will interact more like a body wave with direct shear waves emitted from the rupture on the fault surface than would a dispersive Rayleigh wave in a heterogeneous medium. The Rayleigh wave will directly influence and modify rupture directivity effects in the vicinity of the fault through its interaction with direct and reflected P and S waves (mostly S waves). Apparent horizontal body-wave phase velocities are inversely proportional to fault dip. For a shallow fault dip like 35° , the horizontal apparent velocity of rupture and propagation velocity of S waves are sufficiently fast that Rayleigh waves propagating horizontally toward the fault tip do not overtake the S wave emitted from the rupture front propagating updip. For a steep fault dip like 60° , the horizontal apparent velocity of rupture is half the Rayleigh-wave velocity. The Rayleigh wave propagating along the hanging wall toward the fault tip can arrive in time in the footwall to directly interact with the packet of the direct S wave associated with the updip propagation of rupture or with the wave field associated with the free-surface rupture breakout. The result of interactions of Rayleigh waves and P and S waves will depend on their polarities (more precisely, relative phase relationships), which are determined by the signed radiation patterns associated with the type of dip-slip faulting.

S -wave Interactions with the Free Surface

For shallower angles of incidence associated with shallower fault dips, several phases can propagate as surface and

body waves as well as produce reflected P and S waves that interact with the propagating fault rupture near the free surface. For steeper fault dips, the scattering matrix produces fewer wave types; consequently, a smaller class of waves propagates along the free surface to interact with S waves produced by the fault rupture (Aki and Richards, 1980, p. 142).

Rupture of the Free Surface

Seismic radiation associated with a rupture of the free surface is closely related to Lamb's (1904) problem in which the nondispersive Rayleigh wave is the dominant response resulting from an impulsive force at the free surface. The fault rupture breakout at the free surface produces strong Rayleigh waves that propagate from the fault trace in a fault-normal direction onto the hanging wall and the footwall. In the case of a normal fault, the rupture can jump discontinuously from a point on the fault at depth to the free surface (Nielsen, 1998; Oglesby *et al.*, 1998, 2000). This allows the possibility that all body- and surface-wave phases produced by the breakout phase of the fault surface rupture can interact with upgoing and reflected P and S waves from the rest of the rupture propagating updip.

Interactions of Normal and Shear Stress on Nonvertical Faults

The interactions of normal and shear stresses on dipping faults was the primary focus of Oglesby *et al.* (1998, 2000). They found that dynamic wave interactions between direct and surface-reflected shear waves modified the normal and shear stress at the fault tip at shallow depths, producing distinctly different near-surface rupture behavior between normal- and reverse-slip faulting. In normal-slip faulting, the normal stresses are dynamically reduced along shallow portions of the fault allowing the rupture to discontinuously initiate at or near the free surface and to propagate downdip to intersect the updip rupture from depth. In reverse-slip faulting, the normal stresses are dynamically increased along shallow portions of the fault; this delays rupture initiation until sufficiently high shear stresses initiate rupture. Consequently, large peak slip velocities are associated with shallow reverse-slip faulting relative to shallow normal-slip faulting. A goal of the investigations here is to determine how these dynamic stress factors on the faults systematically influence the peak slip velocities and near-fault peak velocities as a function of the type of faulting.

Peak Velocities as Functions of Dip and Style of Faulting

A 3D model was constructed that was large enough to preclude interactions from artificial boundary reflections with the 3D region of interest near the fault during the time windows of interest. This was necessary because DYNELF does not implement nonreflective boundary conditions. Grid and fault parameters as a function of dip are shown in

Table 1. Initial stresses and final shear stress are shown in Table 2. The various dips were achieved by varying the uniform spacing in the fault-normal and vertical directions to insure the fault intersected the node diagonals at the target dips. The hypocenter depths were varied as a function of dip to produce nearly identical updip rupture widths of ~ 30 km for all dips as indicated in Table 1. Because variable spacing in the x and z directions are used to obtain the target fault dips, this results in slightly wider updip rupture planes for the smallest dips (Table 1). The fault was centered within the grid to increase the time available before artificial reflections returned to the region of interest. All grids had discrete node dimensions of 161 (fault-normal horizontal direction) by 131 (fault-parallel direction) by 131 (vertical direction). Rupture was initiated by applying an initial overstress in a nucleation region with a width of 2 km at the hypocenter.

Figure 1a and b show that fault dip has a strong influence on the location of the largest horizontal fault-normal peak velocities relative to the hanging wall and footwall, particularly in the case of normal faulting. In both types of faulting the maximum peak velocity moves from the hanging wall to the footwall as the dip increases to 50° or more (Fig. 1a and b). In the case of reverse faulting, hanging-wall peak velocities rapidly diminish on the hanging wall near the fault as the dip changes from 50° to 60° (Fig. 1b). In contrast, for normal faulting, the entire lateral breadth of the directivity (horizontal fault-normal component) region switches from the hanging wall for dips of 35° to 41° to the footwall for dips of 49° to 60° (Fig. 1a). Note that the largest peak velocity for the dip of 60° nearly matches the largest peak velocity for a dip of 35° (Fig. 1a). In contrast, the maximum vertical peak velocities remain on the hanging-wall side of the faults, and the amplitude and spatial shape of the peak velocities is nearly independent of dip (Fig. 1d and e). These results are profoundly different from that predicted by ground-motion relations, particularly the recommendations of Abrahamson and Silva (1997) and Somerville *et al.* (1997), who ascribe the dominant amplification of horizontal ground motions associated with directivity to the hanging wall. Abrahamson and Silva (1997) and Somerville *et al.* (1997) did not have a statistically significant sample of near-fault normal-faulting ground motions. Consequently, there is no empirical basis to use the directivity corrections

Table 1

Homogeneous Half-Space Dynamic Rupture Grid Parameters

Dip ($^\circ$)	dx (km)	dy (km)	dz (km)	Zhypo (km)	Width (km)
35	1.000	1.000	0.700	17.5	30.5
38	1.000	1.000	0.780	18.7	30.4
41	1.000	1.000	0.866	19.9	30.4
45	0.866	1.000	0.866	20.8	29.4
47	0.800	1.000	0.866	21.7	29.5
49	0.750	1.000	0.866	22.5	29.8
50	0.725	1.000	0.866	23.4	30.5
55	0.600	1.000	0.866	24.2	29.5
60	0.500	1.000	0.866	26.0	30.0

Table 2
Homogeneous Half-Space Dynamic Rupture Stress Parameters

Static Friction	Dynamic Friction	Yield Shear Stress (Pa)	Initial Shear Stress (Pa)	Final Shear Stress (Pa)	Normal Stress (Pa)
2.532	0.932	0.633	0.43	0.233	0.25

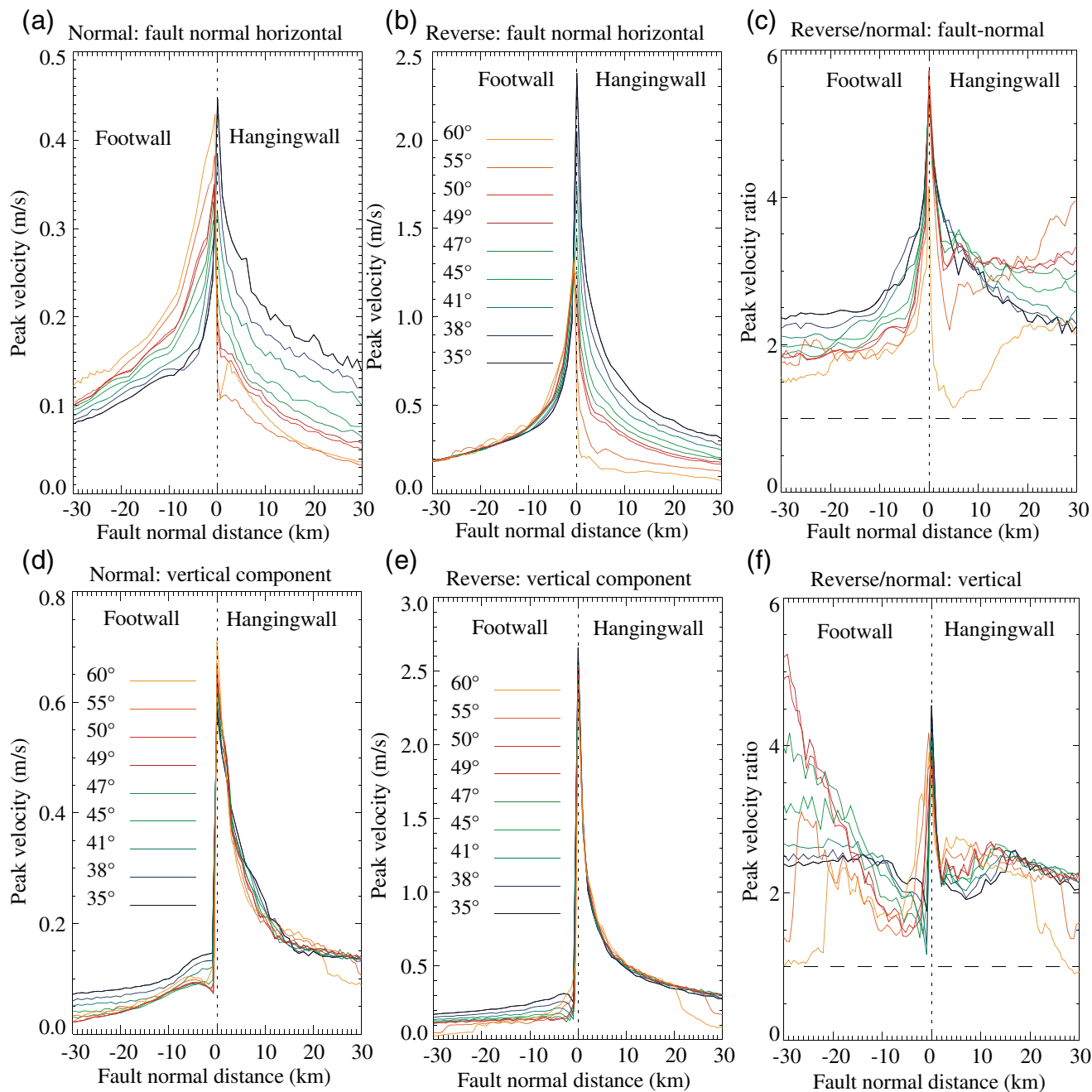


Figure 1. Half-space free-surface peak velocities. (a) Normal and (b) reverse fault-normal horizontal peak velocities. (c) Reverse/normal fault-normal horizontal peak velocity ratios. (d) Normal and (e) reverse vertical peak velocities. (f) Reverse/normal vertical peak velocity ratios. Peak velocity profiles are color coded by dip indicated by the legends in (b), (d), and (e). Vertical dotted lines show fault surface positions. Horizontal dashed lines provides unit references in (c) and (f). Figure 13a illustrates the relationship between fault dip direction and the hanging wall and footwall.

of Abrahamson and Silva (1997) and Somerville *et al.* (1997) for normal faulting. Further, their predictions for reverse faulting are dominated by ground motions recorded from reverse faults with dips $< 50^\circ$. As Figure 1b shows their directivity predictions for fault-normal horizontal ground motions from reverse faulting may also be seriously in error for faults with dips $> 50^\circ$, in cases where crustal velocity structure is relatively homogeneous and topography is relatively subdued.

The other remarkable result noted in detail by Oglesby *et al.* (1998, 2000) is the striking differences in peak velocities between the normal-faulting and reverse-faulting fault-normal horizontal components (Fig. 1c). Reverse-faulting fault-normal peak velocities are always larger than during normal faulting, although the ratios decrease on the hanging wall as fault dip increases (Fig. 1c). In contrast, the lowest ratios of reverse/normal-faulting vertical peak velocity ratios occur on the footwall and are not particularly sensitive to fault dip (Fig. 1f). These results indicate that it may be necessary to consider fault dip in ground-motion prediction relations to obtain realistic estimates of peak-horizontal velocities near dip-slip faults.

Rupture Velocity

Nielsen (1998) and Oglesby *et al.* (1998, 2000) found that in the case of normal faulting in a half-space, the rupture front could bifurcate with one part jumping discontinuously to a point at or near the free surface. This would start a second rupture front that then propagated downdip from the free surface toward the primary updip rupture front. In this case, the kinematics of shear-wave and Rayleigh-wave interactions are changed relative to a single rupture front. The breakout phase associated with rupture of the free surface produces strong body and Rayleigh waves that propagate normal to the fault at an earlier time than Rayleigh waves produced on the hanging wall by the primary updip rupture front. This is investigated as a function of dip using tangent rupture velocities (local gradients) calculated along the strip of the fault updip of the hypocenter (Fig. 2). The large tangent rupture velocities near the free surface in the normal-faulting ruptures are associated with the development of a rupture front at or near the free surface separate from the primary rupture front propagating updip from the hypocenter. As dips approach 60° , the separate rupture front that develops near the free surface involves a narrower region than the shallow dip scenarios like 35° (Fig. 2). Thus, the bifurcated near-surface tangent rupture velocities are lowest for a 60° dip because the dynamic variations of normal stress diminish with increasing dip to zero for a vertical fault (Oglesby *et al.*, 1998, 2000).

Peak Slip Velocities and Accelerations

We extracted slip velocity and acceleration on the fault along a line that is directly updip of the hypocenter. We consider only the updip component of motion for the two

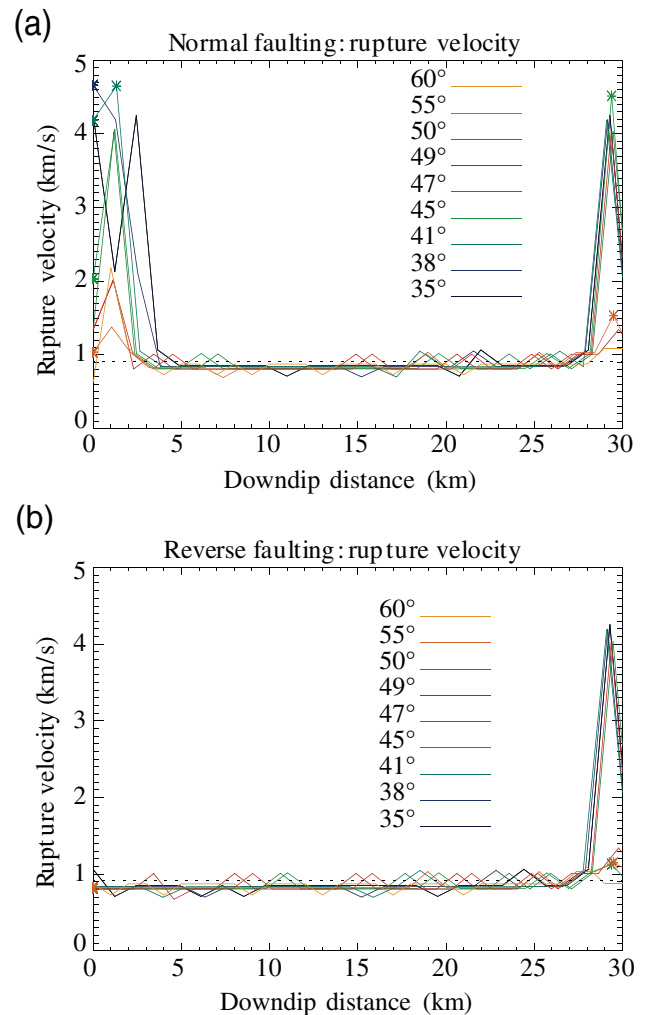


Figure 2. Tangent rupture velocities in the dip-slip direction updip of the hypocenter. (a) Normal-faulting and (b) reverse-faulting results color coded by dip as indicated by the legends. Horizontal dotted lines show 0.91 of the S -wave velocity. Stars are plotted at the discrete positions where tangent rupture velocities are infinite. High rupture velocities are associated with forced initiation of rupture by high initial shear stresses near the hypocenter at the right edges of the plots.

styles of faulting. Normal faulting has moderately larger peak slip velocities near the free surface compared to the downdip portion of the normal faults (Fig. 3a). Reverse faulting has larger peak slip velocity throughout all fault depths than normal faulting (Fig. 3c) but has much larger peak slip velocities near the free surface (Fig. 3b and c). The ratios of reverse-to-normal-faulting slip velocities do not vary strongly with dip (Fig. 3c). Reverse-faulting slip velocities are consistently larger than normal-faulting slip velocities (Fig. 3c). Reverse faulting produces very large slip accelerations near the free surface (Fig. 3e), while normal-faulting slip accelerations actually decrease just below the free surface (Fig. 3d). There is a depth below which peak slip accelerations are nearly the same for both types of faulting

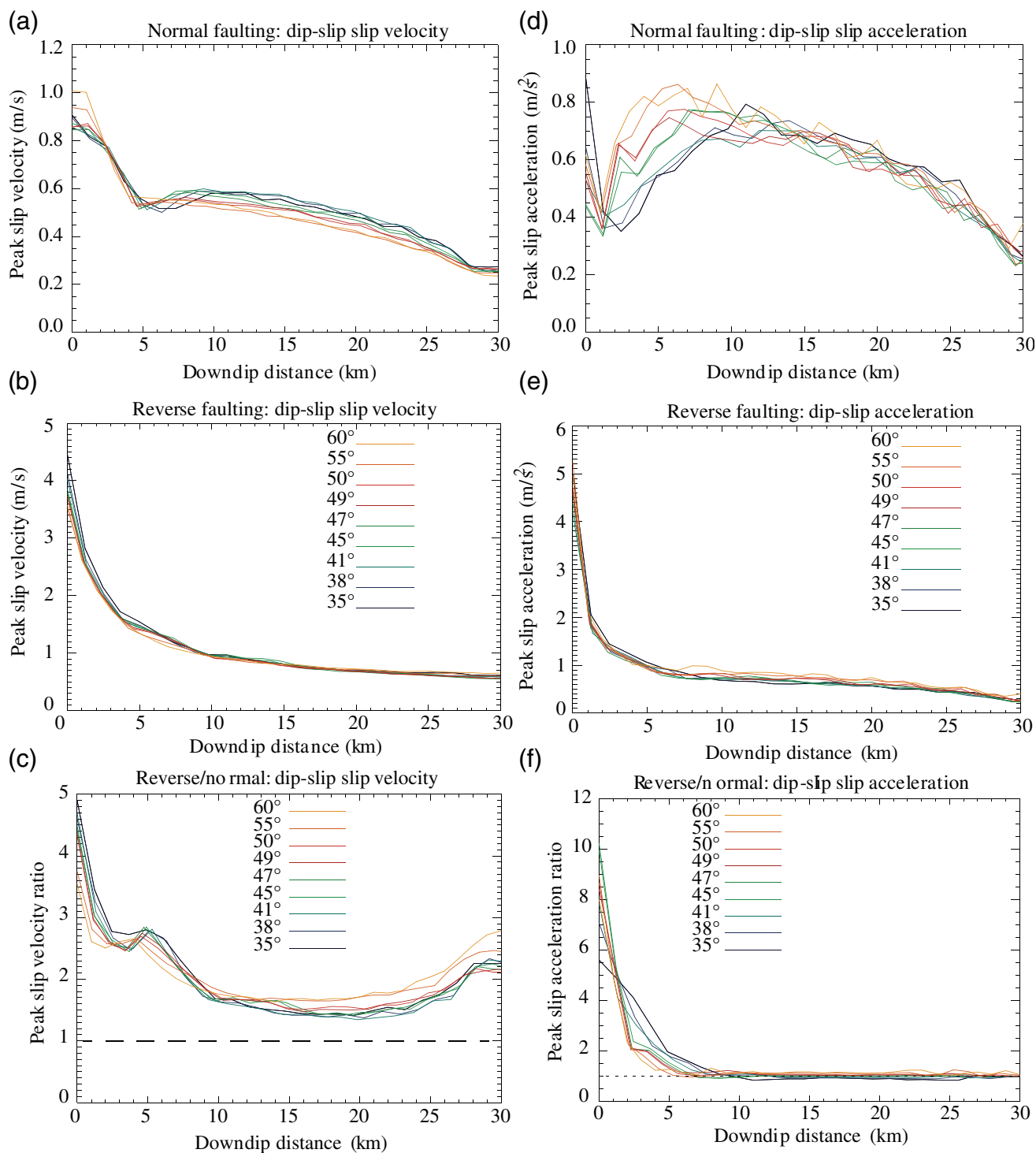


Figure 3. Dip-slip peak slip velocities (a)–(c) and peak slip accelerations (d)–(f) up-dip of the hypocenter. Peak slip velocities for normal faulting (a), reverse faulting (b), and ratios of reverse/normal slip velocities (c). Peak slip accelerations for normal faulting (d), reverse faulting (e), and ratios of reverse/normal slip accelerations (f). Each curve is color coded by its dip as indicated in the legends in (b), (c), (e), and (f).

(Fig. 3f). This indicates that the details of initial conditions near the free surface have a profound impact on peak slip accelerations that strongly influence peak accelerations close to the fault. An increase in fracture energy with decreasing depth (increase of slip-weakening distance near the free sur-

face) would diminish the differences between normal- and reverse-faulting slip velocities and accelerations from shallow portions of fault rupture. However, what is clear is that normal-faulting rupture dynamics systematically reduce or regularize slip velocities and accelerations in the near-surface

region of faulting even when fracture energy is held constant for all rupture depths.

The Near-Fault Propagating Wave Field

The reverse-faulting wave field for a dip of 35° has the most conventional distribution of amplitudes on the hanging wall and footwall (Fig. 4a). The direct S wave precedes the rupture front to the free surface; the largest velocities occur on the hanging wall through constructive interference of S waves and Rayleigh waves. For a dip of 35° the primary difference in the case of normal faulting is that the rupture jumps to the free surface so that there is a broader time window over which the direct S waves, hanging wall Rayleigh wave, and rupture breakout phases interact (Fig. 4b). Consequently, the interference of the phases is not as coherent in time or space so that the region of elevated fault-normal peak velocities is smeared into the footwall (Fig. 1a). In both the reverse- and normal-faulting cases, the hanging-wall S and Rayleigh waves reach the footwall before rupture starts to interfere destructively with the direct S -wave arrivals (Fig. 4a and b). In contrast, for a dip of 60° , the hanging-wall S and Rayleigh waves interfere constructively with the direct S waves on the footwall and destructively on the hanging wall (Fig. 4c and d). The discontinuous jumps of the normal-faulting rupture fronts (Fig. 4b and d) produce a wider time window over which all these phases interfere, producing a broader region over which large amplitudes persist. In the case of normal faulting the discontinuous fault rupture provides a mechanism for reducing the short-period amplitudes of the fault-normal horizontal ground motions. Lateral velocity contrasts across dip-slip faults will clearly modify the kinematics of the near-fault propagating wave field. For instance, a low-velocity normal-fault hanging-wall sedimentary basin may disperse and delay the hanging-wall Rayleigh waves so they can constructively interfere with direct S waves primarily on the hanging wall. The free-surface wave fields in Figure 4 clearly indicate that topography could have a strong influence on near-fault ground motions. Significant topographic relief would scatter surface waves and increase variability of surface-wave travel times. These topographic effects would reduce the tendency for surface waves to constructively interact with S waves in the near-fault region.

Rupture Dynamics in Weakly Heterogeneous Media

We used the 3D finite-element approach of Ma and Archuleta (2006) to evaluate the influences of weak crustal velocity heterogeneity on dynamic rupture of faults dipping 55° . The 1D velocity model appropriate for normal-fault modeling (Fig. 5) was modified to account for first-order random-correlated variations of crustal velocity structure (Frankel and Clayton, 1986; O'Connell, 1999). The 1D velocity model was selected to correspond to velocity structure near the South Fork fault in northern Montana. Velocity randomization parameters listed in Table 3 were selected

to correspond to heterogeneity length scales and velocity variability of Belt Series rocks near the South Fork fault. The velocity randomization approach of O'Connell (1999) was modified to produce self-similar velocity fluctuations. The velocity randomization was used to ensure that first-order S -wave scattering was included that might influence dynamic stresses on the faults and that also influences the amplitude scaling of near-fault ground motions (O'Connell, 1999). 3D grid parameters are given in Table 4. The Resulting velocity variations at the free surface are shown in Figure 6. A depth cross section, taken at 30 km along strike (Fig. 7), shows the reduction in randomization amplitudes with depth required to prevent the P -wave velocity from increasing to values that would require reducing the timestep.

Rupture Model Stochastic Initial Conditions

Two sets of initial shear stresses and static friction fields were used to produce rupture simulations. As discussed in Ma and Archuleta (2006) there are several ways to specify the conditions that control the evolution of fault rupture. Here a constant slip-weakening distance of 0.4 m is used with a constant normal stress of 30 bars. Larger values of slip-weakening distance will reduce radiated seismic energy and ground motions. The objective of these calculations was to compare and contrast normal- and reverse-faulting rupture dynamics and their subsequent ground motions. Thus, the particular choices for these parameters were not critical. However, slip-weakening distance is important for determining the absolute scale of peak ground motions and is not well constrained. In particular, it is possible that slip-weakening distance increases near the free surface (or its increase is a proxy for other mechanisms that reduce seismic radiation [Brodsky and Kanamori, 2001; Andrews, 2002; Ohnaka, 2004; Andrews, 2005]), something not investigated here. Instead, we have reduced strength excesses near the free surface to reduce the influence of the free-surface rupture breakout phase on simulated ground motions. The two sets of initial conditions were produced to provide one nearly bilateral rupture and one nearly unilateral rupture. This allows us to discern the possible influences of hypocenter position along strike on the spatial distribution and polarizations of peak ground motions. Figure 8 shows the initial shear-stress excess and static friction for the bilateral rupture. The initial shear-stress excesses and static frictions differ slightly between the unilateral and bilateral ruptures, with different random seeds used in each case. However, the initial shear stresses were scaled to produce nearly equal stress drops on the order of 32–35 bars for the unilateral and bilateral ruptures and to be consistent with inferred average stress drops for normal-faulting earthquakes in the western United States (Doser and Smith, 1989).

Rupture Simulation Processing

The rupture simulations were performed for durations of 40 sec to capture all the significant rupture and ground-

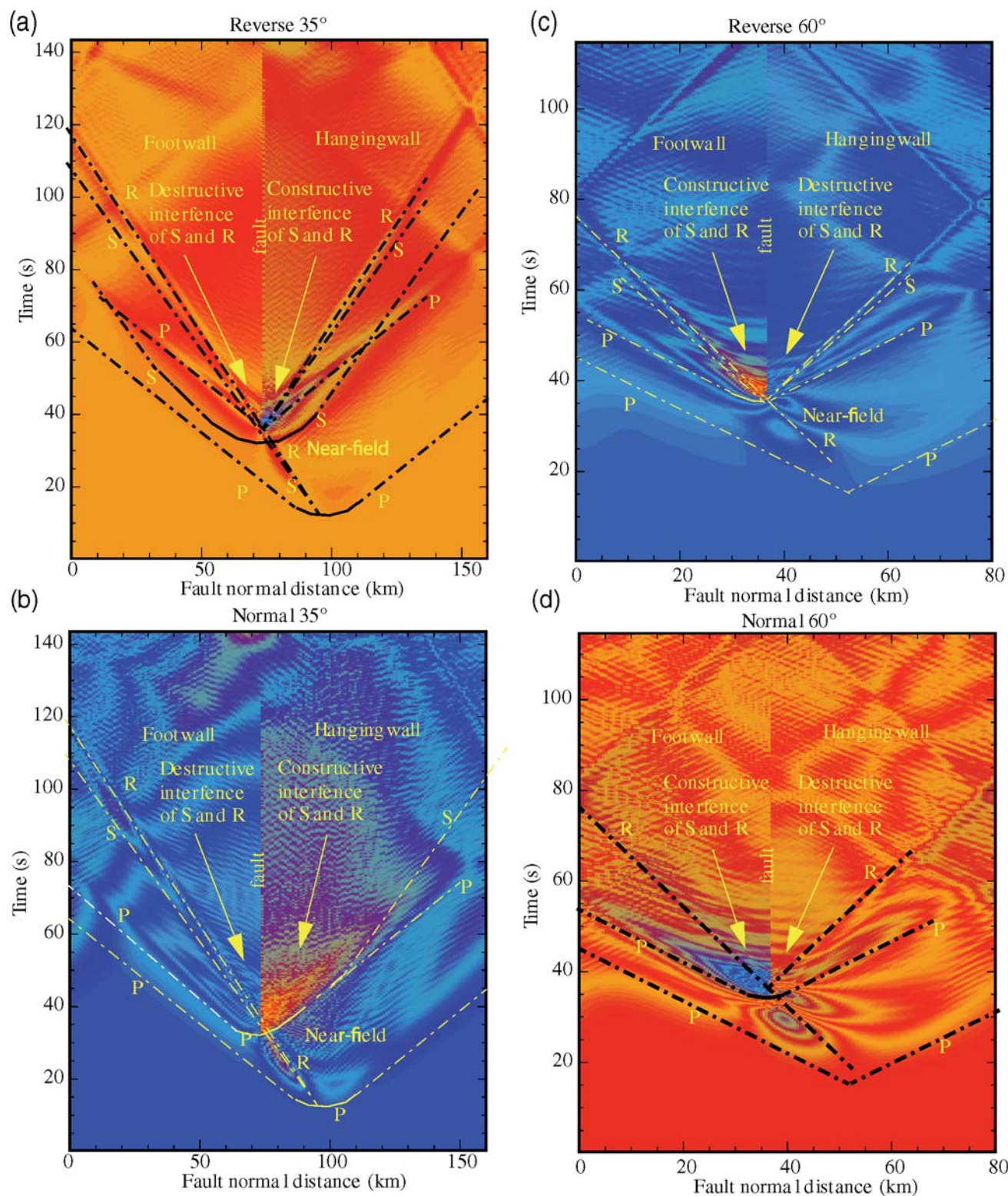


Figure 4. Fault-normal horizontal-component free-surface velocity wave fields for reverse faulting with a dip of 35° (a), 35°-dip normal faulting (b), 60°-dip reverse faulting (c), and 60°-dip normal faulting (d). Maximum amplitudes occur on the hanging wall in (a) in blue and in (b) in orange but occur on the footwall in (c) in orange and in (d) in blue. See Figure 1 for the corresponding peak velocity profiles. Dashed-dotted lines show the dominant P- (P), S- (S), and Rayleigh-wave (R) trains identified using their characteristic phase velocities. Artificial boundary reflections become clear at times of 60 sec or more near the edges of the grid.

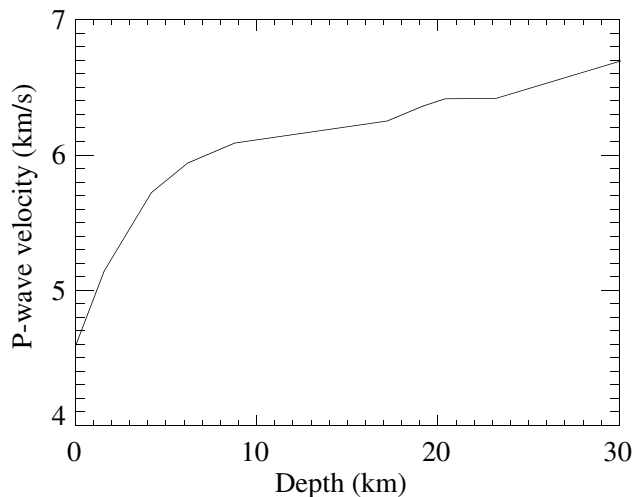


Figure 5. 1D *P*-wave velocity model used in normal- and reverse-faulting rupture simulations.

motion responses. The slip velocities and shear and normal stresses were saved at every timestep (0.0075 sec) at every other node on the fault for both sets of split nodes on the fault. Three-component velocity ground motions at the free surface were saved at every fifth node. Two zero-phase two-pole filters were applied to obtain slip velocities and free-surface ground motions in two distinct frequency bands to quantify differences in the slip velocities and ground motions between normal and reverse faulting at low and high frequencies. A zero-phase two-pole low-pass filter with a 1.0-Hz corner frequency was used to obtain low-frequency slip velocities. A band-pass filter with a passband from 1 to 3.5 Hz (near dispersion limit of the calculations on most of the fault surface) provided high-frequency slip velocities. The dispersion limit for the free-surface ground motions was about 3 Hz. Consequently, two sets of free-surface ground motions were produced using the same low-pass filter (1-Hz corner frequency) and a 1–3 Hz band-pass filter. Rise time was defined as the time for 60% of the slip to occur in order to focus on the time windows associated with initial rupture—the time frame where the peak slip velocities occur almost exclusively.

Rupture Differences: Normal- and Reverse-Faulting Rupture Dynamics

All the pairs of normal and reverse-faulting dynamic rupture calculations used the same initial randomized stresses and static frictions, only the sign of the initial shear stresses was reversed. Systematic differences in normal- and reverse-fault peak slip velocities are clearly apparent for all depths (Fig. 9a and b) but are strongest within 5 km of the free surface. The differences are much clearer in terms of ratios (Fig. 9c and d). Up to the 84% fractile normal-faulting slip velocities are never larger than their reverse-faulting counterparts for the same initial conditions. More striking

Table 3

3D Crustal Velocity Randomization Parameters		
Correlation Length (km)	Standard Deviation	Hurst Exponent
2.5	5%	Self-similar

is that the normal-faulting slip velocities for frequencies of 1–3.5 Hz are, on average, 72% of their reverse-faulting counterparts (Fig. 9c). The large slip velocities near the free surface are the result of the rupture breakout phase, which produces large motions close to the fault. Yet, it is remarkable that even with a seismogenic breakout phase, the largest normal-faulting slip velocities near the free surface are < 1 m/sec for the 1–3.5 Hz frequency band (Fig. 9a) and less than 2 m/sec in the < 1 Hz frequency band (Fig. 9b). In contrast, the reverse-faulting near-surface peak slip velocities actually are larger in the 1–3.5 Hz frequency band (Fig. 9a) than at frequencies < 1 Hz (Fig. 9b). On average, reverse-faulting slip velocities were 39% larger than those for normal faulting in the 1–3.5 Hz frequency band, but on average, reverse-faulting slip velocities were only 16% larger than normal-faulting slip velocities for frequencies < 1 Hz. This indicates that normal-faulting ground motions may have maximum spectral accelerations at distinctly lower-frequencies than that for reverse-faulting ground motions.

The spatial patterns of rise-time ratios illustrate the impact of the differences in the dynamic interactions that occur between shear and normal stresses when contrasting normal and reverse faulting. Rise-time differences are most profound near the free surface but persist to depths of nearly 15 km (Fig. 10). While normal-faulting slip velocities are systematically smaller than reverse-fault slip velocities (Fig. 9), nearly identical final slips are produced. This happens because the normal-faulting rise times increase with decreasing depth in nearly the same manner (Fig. 10) as the normal-faulting slip velocities decrease relative to reverse-faulting slip velocities (Fig. 9). The much longer near-surface normal-faulting rise times, which are nearly five times longer than corresponding reverse-faulting rise times, allow much smaller near-surface slip velocities to produce nearly identical final slips as reverse faulting. The early nucleation of rupture at the free surface that occurs during normal faulting contributes to the increased normal-faulting rise times near the surface. The early nucleation rupture that proceeds down-dip during normal faulting is antidirective, which further reduces the influence of shallow fault rupture on near-fault normal-faulting ground motions. Thus, normal faulting pro-

Table 4

3D Randomized Velocity Dynamic Rupture Grid Parameters		
Strike Nodes/Spacing (km)	Depth Nodes/Spacing (km)	Fault-Normal Nodes/Spacing (km)
600 (0.1)	260 (0.1)	380 (0.07)

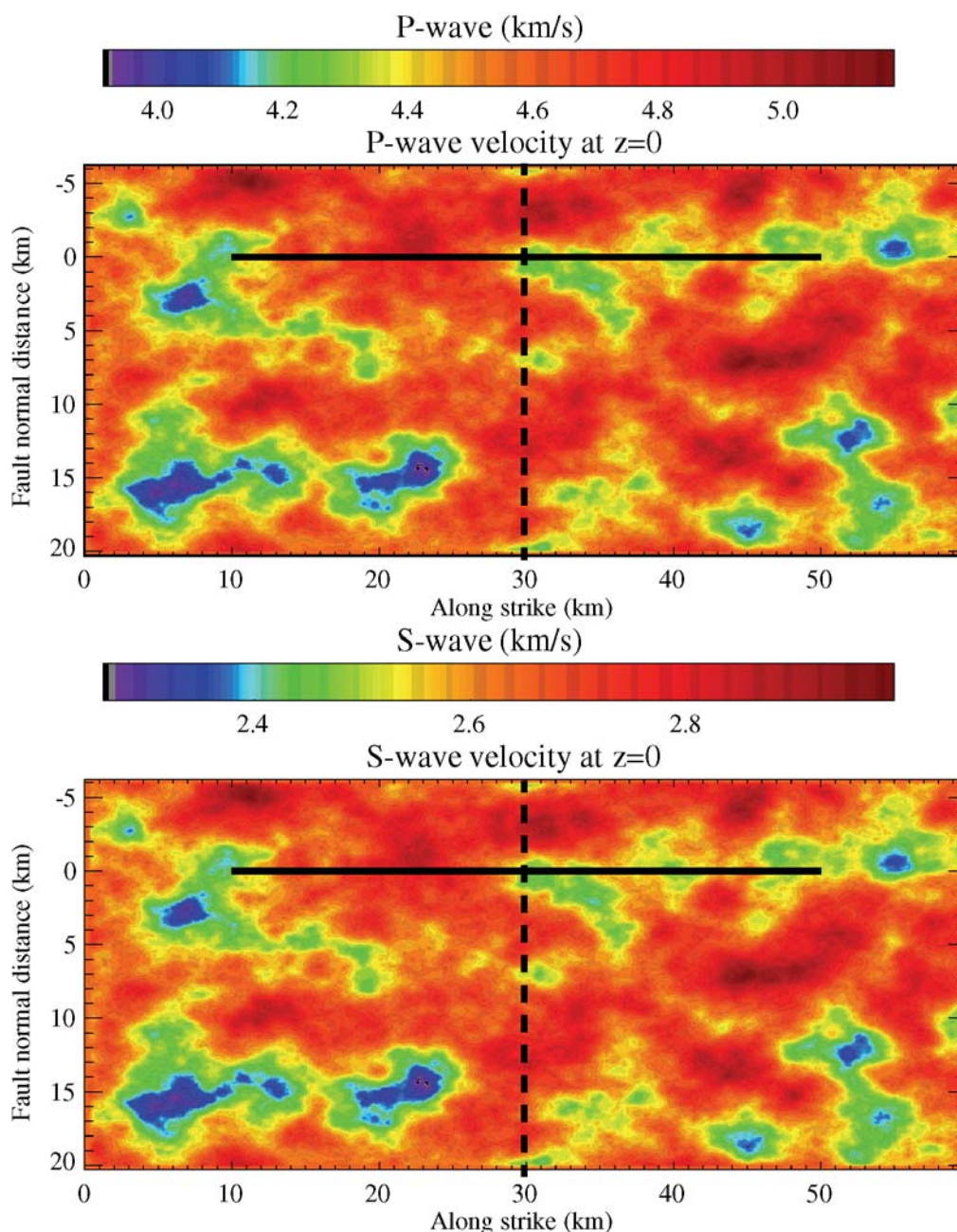


Figure 6. Free-surface P - and S -wave velocities for the 3D rupture model. Solid lines show the surface position of the 40-km-long fault position used in the simulations. Positive fault-normal distances correspond to the hanging wall. Dashed lines indicate positions of the depth sections in Figure 7.

duces more benign ground motions at frequencies > 1 Hz because slip occurs slower (Fig. 9), and near the surface slip is split into pulses that are distinct in time (simultaneous updip and downdip rupture), and one pulse of slip is anti-directional for surface sites.

Near-Fault Ground Motions

Figure 11 provides examples of free-surface velocity waveforms from the unilateral rupture. The largest fault-

normal peak-horizontal velocities occur on the footwall, while large peak vertical velocities occur on the hanging wall, indicating that weak lateral and vertical velocity heterogeneity does not strongly change the results from those obtained in a uniform half-space (at low frequencies, Fig. 12a–d). However, at higher frequencies of 1–3 Hz (Fig. 12e and f) the largest fault-normal peak velocities extend several kilometers onto the hanging wall during both normal and reverse faulting. Shallow strike-slip components of fault rupture that

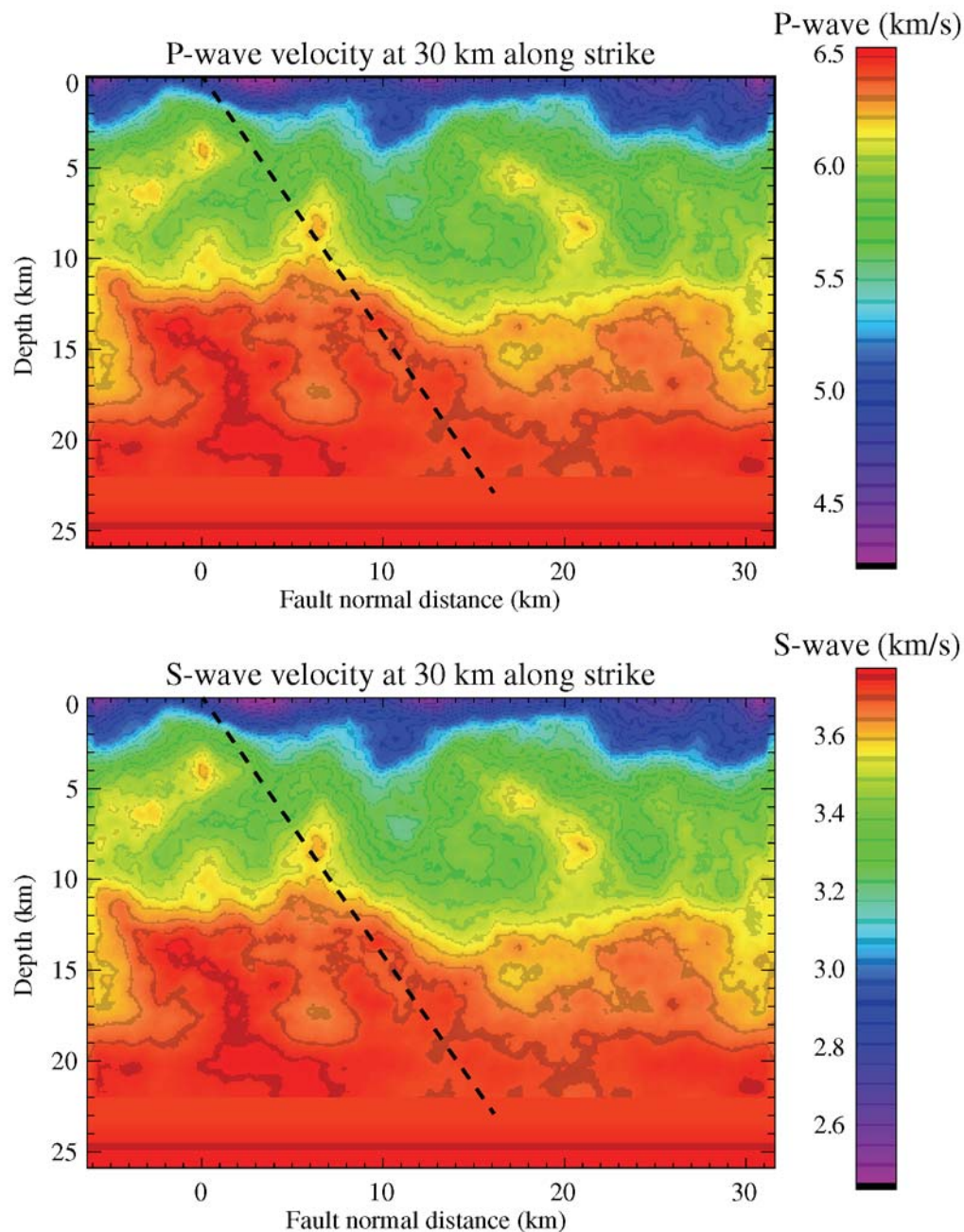


Figure 7. *P*- and *S*-wave fault-normal depth sections from the 3D rupture model at 30 km along strike. Dotted lines show the subsurface position of the fault.

occur near the ends of the fault rupture can produce substantial fault-parallel peak velocities. These are mostly confined to the hanging wall along the fault trace but can extend onto the footwall beyond the ends of the fault (Fig. 12c and d). At higher frequencies (1–3 Hz) the large fault-parallel peak velocities occur near the fault on both the footwall and hanging wall, but with a bias for substantial peak velocities to extend further onto the hanging wall (Fig. 12g). In contrast, for reverse faulting the largest higher frequency fault-normal peak velocities are confined to the hanging wall (Fig. 12h).

Normal Faulting on a Bimaterial Fault Interface Dipping 55°

Harris and Day (1997) were the first to numerically study bimaterial (and trimaterial) spontaneous rupture scenarios using slip-weakening friction using a 2D in-plane formulation. Harris and Day (1997) investigated vertical strike-slip faulting and presented analytical and spontaneous rupture solutions for in-plane rupture. Harris and Day (2005) simulated the full 3D problem of vertical strike-slip rupture, including both in-plane and antiplane rupture, and simulated

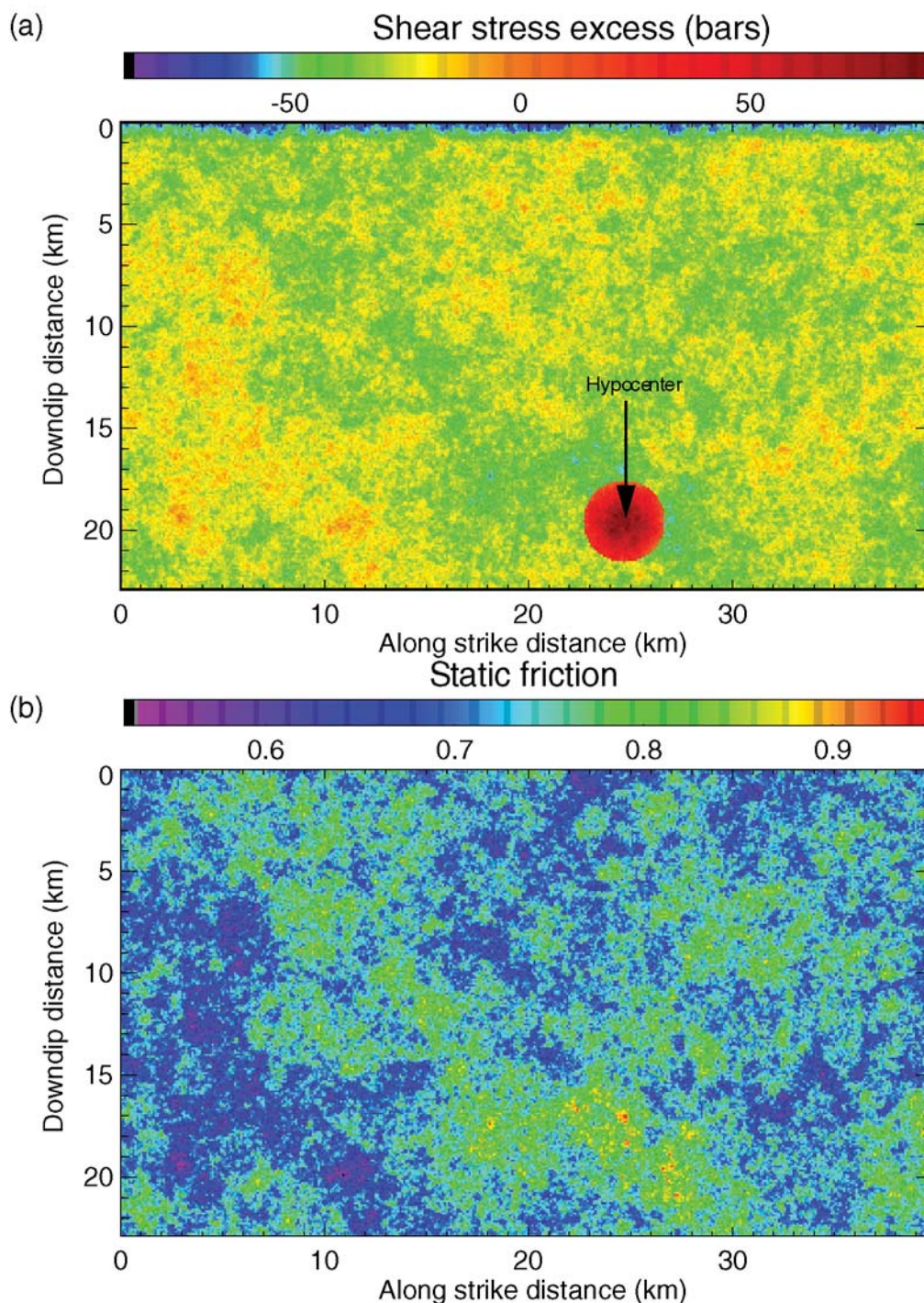


Figure 8. Initial bilateral shear-stress excess (a) and static friction (b) distributions on the fault.

a 3D bimaterial case that indicated that material contrast is unlikely to induce a preferred rupture direction. Here we examine a corresponding 3D bimaterial problem for a normal faulting dipping 55° .

We used a 3D velocity model derived from O'Connell *et al.* (2003) for the Teton normal fault in Wyoming to provide an illustration of the effect of a shallow “bimaterial”

fault interface on hanging wall and footwall ground motions. We use the term “bimaterial” here to refer to two general types of materials, hanging-wall material consisting of lower-velocity sediments with velocities corresponding to a compaction profile and footwall material consisting of nearly homogenous high-velocity basement rocks. The velocity model has a three-to-one shear-wave velocity contrast

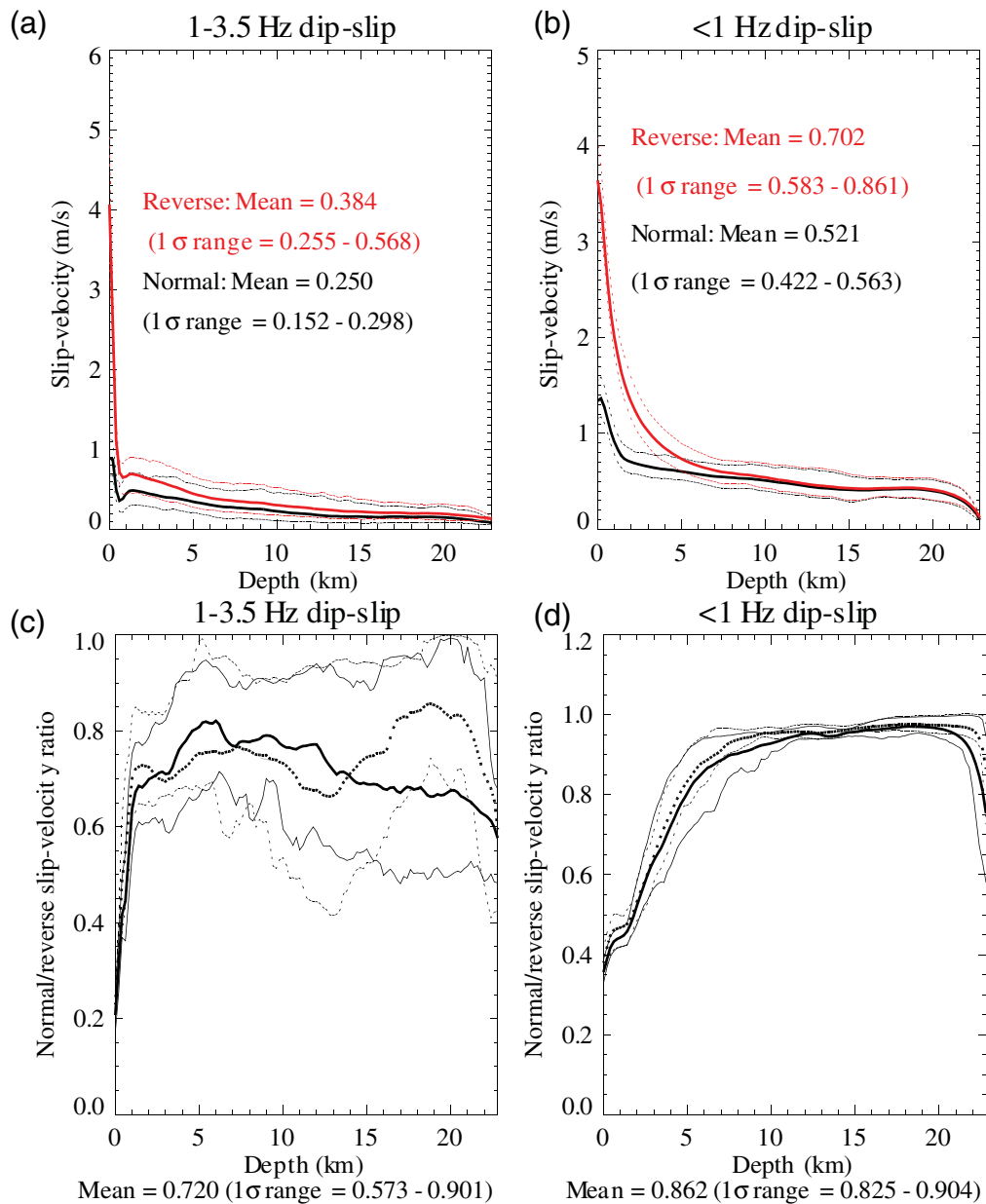


Figure 9. High-frequency (a) and low-frequency (b) peak slip velocities as a function of depth and type of faulting. Solid lines are means with red for reverse faulting and black for normal faulting. Dotted lines are 16% and 84% limits color coded the same way as the means. Corresponding reverse/normal ratios are shown in (c) for high frequencies and (d) for low frequencies. Thick solid and dotted lines represent the mean results at each depth from the two rupture simulations. Thin lines are 16% and 84% limits with same line styles as the means.

at the surface between hanging-wall sediments and foot-wall rock. This contrast diminishes with increasing depth (Fig. 13a). S. Ma and G. C. Beroza (unpublished manuscript, 2007) showed that both the material contrast in this case and the free surface interact constructively on the normal stress on the fault, leading to a smaller stress drop near the free surface. We simulate a normal-faulting rupture that is 40 km along strike. We impose a stochastic initial shear stress and static friction with properties similar to Andrews (1981). The node spacing is 100 m with a 1.0-Hz frequency

dispersion limit. Maps of peak velocity show that the largest peak velocities are limited to the hanging wall for all ground-motion components (Fig. 13b–d). However, substantial fault-normal horizontal peak velocities on the order of 0.5–1.0 m/sec occur on the footwall within 2 km of the fault (Fig. 13b). Thus even strong bimaterial fault interfaces, typical of normal faults in the Basin and Range and Intermountain regions of the western United States, do not preclude significant fault-normal velocities on the footwall for faults dipping up to 55°.

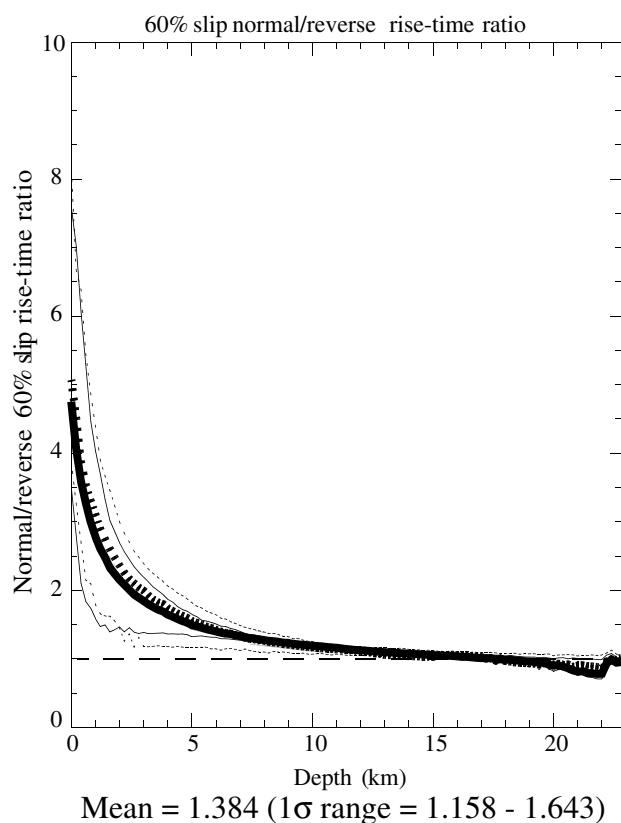


Figure 10. Ratios of normal-to-reverse-faulting peak rise times as a function of depth. Thick solid and dotted lines represent the mean results at each depth from the two rupture simulations (unilateral and bilateral). Thin lines are 16% and 84% limits with same line styles as the means. Horizontal dashed lines provide unity reference.

The largest footwall fault-normal peak velocities may be limited to lower frequencies because shorter period energy would refract toward the hanging wall. The solution for a point source embedded on a bimaterial interface (Ben-Zion, 1990, 1999) is used here to show that much smaller particle velocities occur close to the fault below the free surface on the footwall side for the geometry in Figure 13a relative to hanging-wall positions at the same distance from the fault. Free-surface effects are ignored in the exact solution of Ben-Zion (1990, 1999) for two uniform half-spaces in welded contact. Consequently, our results suggest first-order seismic radiation effects at depths of 1–3 km relevant to the 3D crustal structure developed in Figure 13a. The shear dislocation on the vertical fault in Figure 14 is in the dip (z) direction. We consider three sets of receiver positions—all located 100 m from the fault at three distances along the strike of the fault. The velocity configuration is shown in Figure 14. Simulation parameters are in Table 5. We show results for the fault-normal (x) horizontal component, although similar results are obtained for the fault-parallel (y) component.

At the observer position closest to the point source and nearly normal to the updip projection of the fault (10-m updip), the slow side amplitudes are generally much larger than the fast side at nearly all frequencies (Fig. 15a and d). P -wave energy is substantial, particularly on the slow side; this complicates the spectral responses ratios for the sites close to the point source (Fig. 15a). In contrast, once the receivers are at least 500-m updip, S -wave arrivals are much larger than the P -wave arrivals, and the large amplitudes of the slow side relative to the fast side are readily apparent at increasing frequencies. At frequencies of 3 Hz or more, slow side fault-normal amplitudes are more than 10 times larger than fast side amplitudes (Fig. 15b and e). The trend continues for the receivers 1000-m updip of the point source (Fig. 15c and f). The steady decrease in fast side peak velocities with increasing updip distance reflects the progressive loss of energy from the fast side to the slow side through headwaves traveling along the interface (Ben-Zion, 1990, 1999). Thus, it appears likely that most of the footwall fault-normal peak velocities in Figure 13b will be associated with frequencies < 1 Hz because the bimaterial interface head waves effectively filter out higher frequency energy from the footwall. Dynamic rupture calculations with a finer mesh will be necessary to determine if that is indeed the case.

Discussion

The calculations used here do not account for viscoelastic damping. These elastic numerical solutions include wave-field components with a wavelength too short to be modeled accurately by grid-based numerical methods. Consequently, it is important not to ascribe too much significance to the absolute amplitudes obtained from these calculations. The primary focus is on first-order differences between reverse- and normal-faulting rupture dynamics and on near-fault ground motions in terms of slip velocity and near-fault peak velocities.

Strong lateral velocity contrasts across the top several kilometers of a normal fault dipping 55° are required to reduce footwall fault-normal peak velocities relative to the cases of a homogeneous half-space and weakly heterogeneous correlated-random velocity variations with modest vertical velocity gradients. However, other factors may significantly disrupt the symmetries involved in the rupture of planar faults in homogeneous or weakly heterogeneous media. Topography will scatter and modify the kinematics and amplitudes of near-fault surface waves (Ma *et al.*, 2007). In particular, surface waves associated with rupture breakout are likely to interfere less constructively and less consistently with body waves in rugged terrain typically associated with the footwall region of normal faults and the hanging-wall region of reverse faults. Nonplanar fault geometries will complicate wave kinematics through travel-time and rupture-time variability associated with bends (Kase and Day, 2006) and segmentation (Oglesby *et al.*, 2003).

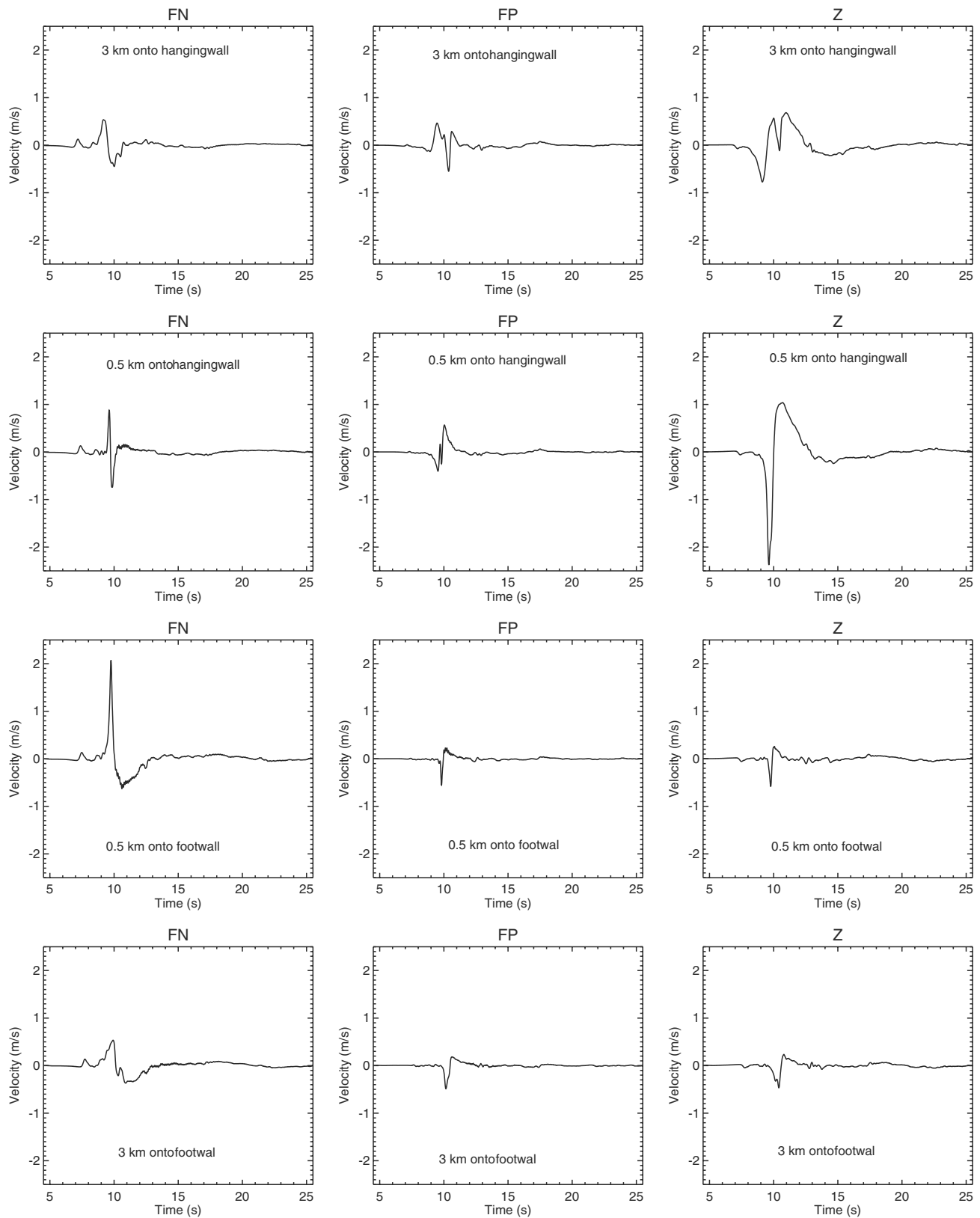


Figure 11. Three-component (fault normal, FN; fault parallel, FP; and vertical, Z) band-pass filtered free-surface velocity waveforms from the unilateral normal-faulting rupture at distances of 0.5 and 3 km from the fault on both the hanging wall (top two sets of three-component waveforms labeled HW) and the footwall (bottom two sets of three-component waveforms labeled FH) at a strike position of 37.5 km in the coordinates of Figure 12.

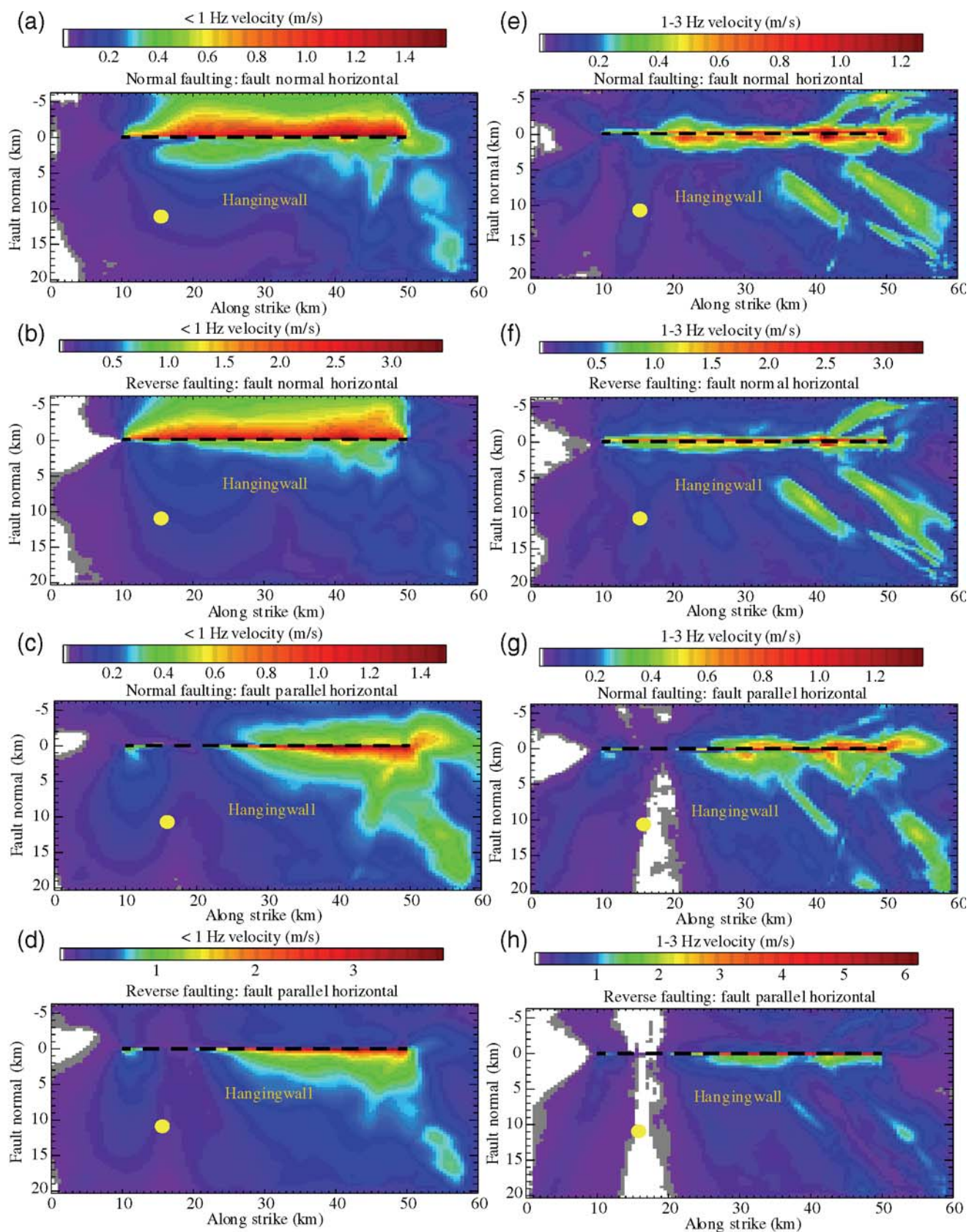


Figure 12. Plan views of 55° -dip unilateral < 1 Hz peak-horizontal velocities (a)–(d) and 1–3-Hz peak-horizontal velocities (e)–(h). Normal-faulting cases are (a), (c), (e), and (g). Reverse-faulting cases are (b), (d), (f), and (h). Fault-normal components are (a), (b), (e), and (f). Fault-parallel components are (c), (d), (g), and (h). Dashed black lines show the surface extent of the fault. Epicenters are yellow dots; hypocenter depth was 19.6 km.

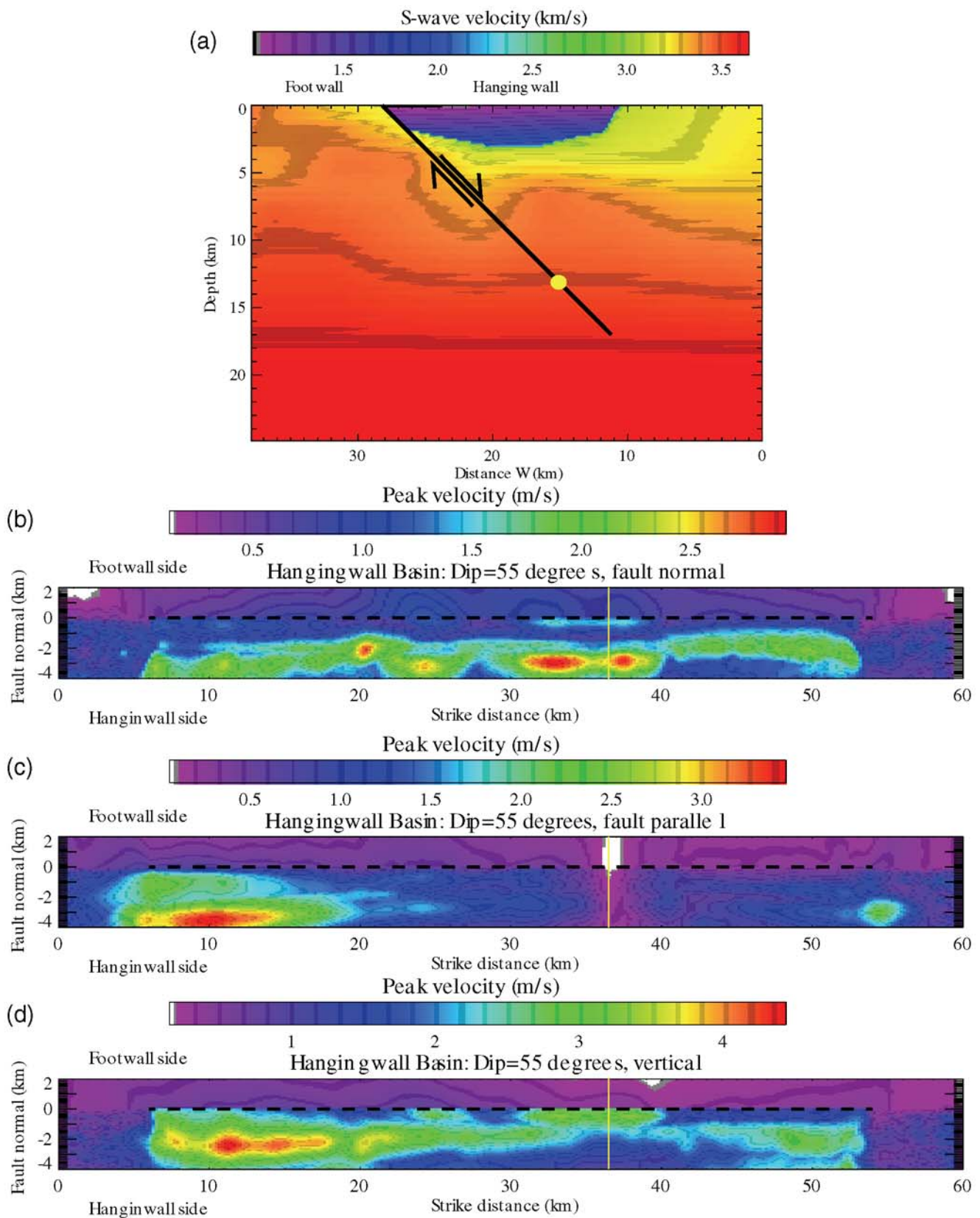


Figure 13. S-wave velocity model cross section (a) and 55°-dip peak velocity maps (b) and (c). In (a) the solid black line is the Teton fault (shown dipping 45°). The node spacing in the fault-normal direction was reduced from 100 to 70 m to increase the dip on the fault from 45° to 55°. In the plan views of peak velocity (b) and (c) the dashed lines are the surface trace of the Teton fault. The hypocenter was placed at a strike position of 36.5 km at a depth of 13.5 km, as indicated by the yellow dot in (a) and the yellow vertical lines in (b)–(d).

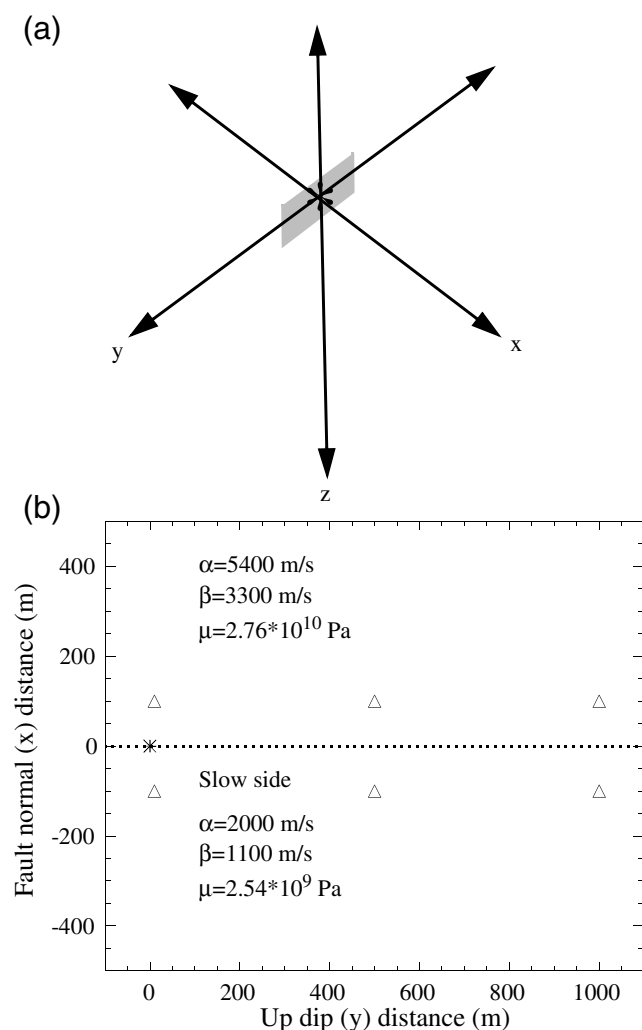


Figure 14. Whole-space bimaterial fault geometry. (a) Coordinate system with the fault plane dipping 90° in the y - z plane (shaded region shows orientation) and the point source at the origin (star). (b) Plan view with the point source at the origin (star), the dotted line indicates the fault and bimaterial interface, receiver positions are the triangles, and the material parameters on each side are listed.

We used slip weakening with a single scalar slip-weakening distance imposed over entire fault surfaces. It appears quite likely that shallow material, particularly basin fills, should have different rupture characteristics than rocks found in the middle to lower crust. For instance, rupture may become spread over a finite damage zone in softer near-surface rocks/sediments. Such nonelastic responses could limit slip velocities from shallow portions of rupture (Andrews, 2005). However, even with uniform slip-weakening distances employed in these elastic calculations, which implies no increase in fracture energy in the shallow portion of rupture, normal-faulting rupture dynamics within several kilometers of the free surface serve to regularize slip velocities through the interaction of shear and normal stress (Oglesby *et al.*, 1998, 2000; S. Ma and G. C. Beroza, unpub-

Table 5

Point-Source Bimaterial
Simulation Parameters

Parameter	Value
Timestep (sec)	0.0005
Total time (sec)	2
Displacement ramp rise time (sec)	0.01
Along-dip dislocation (m)	0.14

lished manuscript, 2007.). This leads to relatively modest free-surface peak velocities for the cases considered here.

Conclusions

Dynamic rupture simulations indicate that near-fault fault-normal peak velocities are sensitive to fault dip. In homogeneous and weakly heterogeneous media with faults dipping less than $\sim 50^\circ$, the maximum fault-normal hanging-wall peak velocities occurred on the hanging wall. However, for fault dips greater than $\sim 50^\circ$, maximum fault-normal peak-horizontal velocities occurred on the footwall. For all dips (35° – 60°) the maximum fault-parallel and vertical peak velocities were observed on the hanging wall. Two rupture simulations in weakly heterogeneous media found that in the 1–3.5-Hz frequency band reverse-faulting slip velocities were on average 39% larger than during normal faulting, but for frequencies less than 1.0 Hz on average reverse-faulting slip velocities were only 16% larger than normal-faulting slip velocities. This indicates that normal-faulting ground motions may have peak spectral accelerations at distinctly lower frequencies than reverse-faulting ground motions. A 3D velocity model with a low-velocity basin (several kilometers in thickness) with a three-to-one shear-wave velocity contrast across a fault dipping 55° generated reduced normal-faulting fault-normal peak velocities on the footwall relative to homogeneous and weakly heterogeneous velocity models. The sediments on the hanging wall of the normal fault tend to lower the stress drop on the fault near the surface (S. Ma and G. C. Beroza, unpublished manuscript, 2007). However, substantial (0.5–1 m/sec) fault-normal peak velocities remained on the footwall, while maximum fault-normal peak-horizontal velocities occurred on the more compliant hanging wall.

These calculations represent an intermediate step toward better understanding of near-fault ground-motion hazards associated with dip-slip faulting associated with a wide range of fault dips. They do suggest that simple hanging-wall/footwall parameterizations in ground-motion prediction relations like Abrahamson and Silva (1997) may yield inappropriate predictions for near-fault footwall sites for faults with dips greater than $\sim 50^\circ$. Further, as Figures 11 and 12 indicate, fault-parallel peak velocities may dominate fault-normal velocities on the hanging wall of reverse faults dipping $\sim 50^\circ$ in a manner not envisioned in the ground-motion polarization and amplitude prediction scheme of Somerville *et al.* (1997). To quantify near-fault peak velocities that are

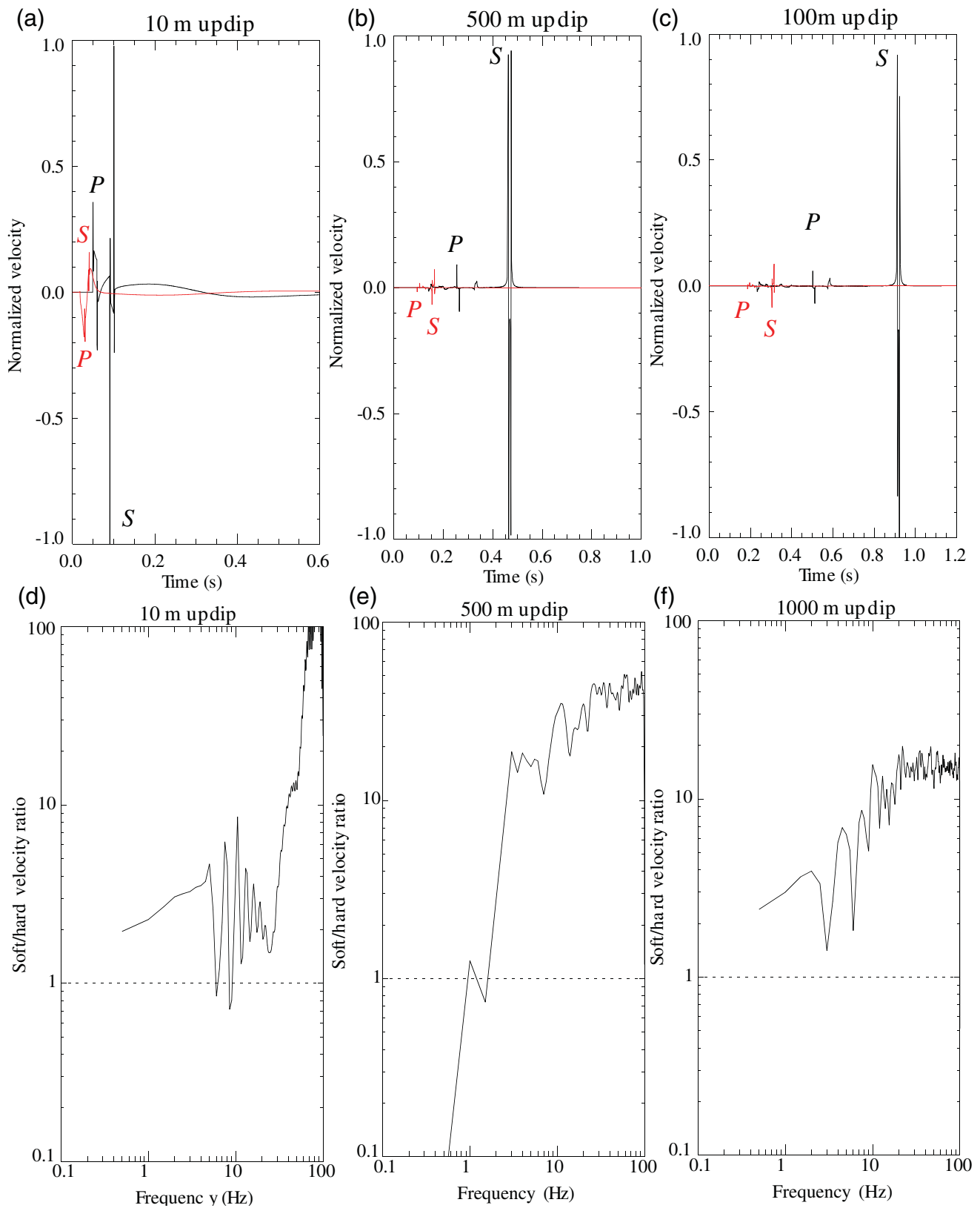


Figure 15. Fault-normal motions at 10-m (a), 500-m (b), and 1000-m (c) updip distance and corresponding slow/fast spectral ratios (d)–(f). Fault-normal particle velocities are normalized relative to slow side maximum amplitudes in (a)–(c) with slow side responses in black and fast side in red.

likely to occur during normal-faulting earthquakes dynamic rupture calculations that incorporate linear and/or nonlinear damping, topography, realistic 3D velocity variations, and fault geometric complexities are needed in light of the sparse normal-faulting near-fault strong motion data currently available.

Acknowledgments

D. J. Andrews kindly provided his DYNELF software. Y. Ben-Zion kindly provided his bimaterial synthetic seismogram software. Financial support provided under the RUPTU and SITER projects of Reclamation's Dam Safety Research Program. Ruth Harris, David Oglesby, and an anonymous reviewer provided helpful reviews that improved the paper. This research was supported by the Southern California Earthquake Center (SCEC). The SCEC is funded by National Science Foundation (NSF) Cooperative Agreement Number EAR-0106924 and by U.S. Geological Survey Cooperative Agreement Number 02HQAG0008. The SCEC contribution number for this article is 1100. This is Institute for Crustal Studies (ICS) Contribution Number 0809 and ICS Contribution Number 813.

References

- Abrahamson, N. A., and W. J. Silva (1997). Empirical response spectral attenuation relations for shallow crustal earthquakes, *Seism. Res. Lett.* **68**, 94–127.
- Aki, K., and P. Richards (1980). *Quantitative Seismology, Theory and Methods*, W. H. Freeman, New York, 557 pp.
- Ambraseys, N. N., J. Douglas, P. Smit, and S. K. Sarma (2005). Equations for the estimation of strong ground motions from shallow crustal earthquakes using data from Europe and the Middle East: horizontal peak ground acceleration and spectral acceleration, *Bull. Earthq. Eng.* **3**, 1–53.
- Andrews, D. J. (1981). A stochastic fault model, 2. Time-dependent case, *J. Geophys. Res.* **86**, 10,821–10,834.
- Andrews, D. J. (1999). Test of two methods for faulting in finite-difference calculations, *Bull. Seismol. Soc. Am.* **89**, 931–937.
- Andrews, D. J. (2002). A fault constitutive relation accounting for thermal pressurization of pore fluid, *J. Geophys. Res.* **107**, 2363, doi 10.1029/2002JB001942.
- Andrews, D. J. (2005). Rupture dynamics with energy loss outside the slip zone, *J. Geophys. Res.* **110**, B01307, doi 10.1029/2004JB003191.
- Ben-Zion, Y. (1990). The response of two half spaces to point dislocations at the material interface, *Geophys. J. Int.* **101**, 507–528.
- Ben-Zion, Y. (1999). Corrigendum to “The response of two half spaces to point dislocations at the material interface” by Ben-Zion (1990), *Geophys. J. Int.* **137**, 580–582.
- Bernard, P., and A. Zollo (1989). The Irpinia (Italy) 1980 earthquake: detailed analysis of a complex normal faulting, *J. Geophys. Res.* **94**, 1631–1647.
- Brodsky, E. E., and H. Kanamori (2001). The elastohydrodynamic lubrication of faults, *J. Geophys. Res.* **106**, 16,357–16,374.
- Brune, J. (1996). Particle motions in a physical model of shallow angle thrust faulting, *Proc. Indian Acad. Sci. (Earth Planet Sci.)* **105**, L197–L206.
- Doser, D. I., and R. B. Smith (1989). An assessment of source parameters of earthquakes in the cordillera of the western United States, *Bull. Seismol. Soc. Am.* **79**, 1383–1409.
- Frankel, A., and R. W. Clayton (1986). Finite difference simulations of seismic scattering: implications for the propagation of short-period seismic waves in the crust and models of crustal heterogeneity, *J. Geophys. Res.* **91**, 6465–6489.
- Harris, R. A., and S. M. Day (1997). Effects of a low-velocity zone on a dynamic rupture, *Bull. Seismol. Soc. Am.* **87**, 1267–1280.
- Harris, R. A., and S. M. Day (2005). Material contrast does not predict earthquake rupture propagation direction, *Geophys. Res. Lett.* **32**, L23301, doi 10.1029/2005GL023941.
- Hudson, J. A. (1980). *The Excitation and Propagation of Elastic Waves*, Cambridge U Press, Cambridge, 224 pp.
- Johnson, L. R. (1974). Green's function for Lamb's problem, *Geophys. J. R. Astr. Soc.* **37**, 99–131.
- Kase, Y., and S. M. Day (2006). Spontaneous rupture processes on a bending fault, *Geophys. Res. Lett.* **33**, L10302, doi 10.1029/2006GL025870.
- Lamb, H. (1904). On the propagation of tremors over the surface of an elastic solid, *Philos. Trans. R. Soc. London, Ser. A* **203**, 1–42.
- Ma, S., and R. J. Archuleta (2006). Radiated seismic energy based on dynamic rupture models of faulting, *J. Geophys. Res.* **111**, B05315, doi 10.1029/2005JB004055.
- Ma, S., R. J. Archuleta, and M. T. Page (2007). Effects of large-scale surface topography on ground motions, as demonstrated by a study of the San Gabriel Mountains, Los Angeles, California, *Bull. Seismol. Soc. Am.* **97**, 2066–2079.
- Nielsen, S. B. (1998). Free surface effects on the propagation of dynamic rupture, *Geophys. Res. Lett.* **25**, 125–128.
- O'Connell, D. R. H. (1999). Replication of apparent nonlinear seismic response with linear wave propagation models, *Science* **283**, 2045–2050.
- O'Connell, D. R. H., C. K. Wood, D. A. Ostenaar, L. V. Block, and R. C. LaForge (2003). Seismotectonic Report 2003-2, Ground motion evaluation for Jackson Lake Dam, Minidoka Project, Wyoming, U.S. Bureau of Reclamation, Denver, Colorado, 468 pp.
- Oglesby, D. D., R. J. Archuleta, and S. B. Nielsen (1998). Earthquakes on dipping faults: the effects of broken symmetry, *Science* **280**, 1055–1059.
- Oglesby, D. D., R. J. Archuleta, and S. B. Nielsen (2000). The three-dimensional dynamics of dipping faults, *Bull. Seismol. Soc. Am.* **90**, 616–628.
- Oglesby, D. D., S. M. Day, and D. R. H. O'Connell (2003). Dynamic and static interaction of two thrust faults: a case study with general implications, *J. Geophys. Res.* **108**, 2489, doi 10.1029/2002JB002228.
- Ohnaka, M. (2004). A constitutive scaling law for shear rupture that is inherently scale-dependent, and physical scaling of nucleation time to critical point, *Pure Appl. Geophys.* **161**, 1915–1929.
- Shi, B., A. Anoushehpour, J. N. Brune, and Y. Zeng (1998). Dynamics of thrust faulting: 2D lattice model, *Bull. Seismol. Soc. Am.* **88**, 1484–1494.
- Somerville, P. G., N. F. Smith, R. W. Graves, and N. A. Abrahamson (1997). Modification of empirical strong ground motion attenuation relations to include the amplitude and duration effects of rupture directivity, *Seism. Res. Lett.* **68**, 199–222.
- Spudich, P., W. B. Joyner, A. G. Lindh, D. M. Boore, B. M. Margaris, and J. B. Fletcher (1999). SEA99: a revised ground motion prediction relation for use in extensional tectonic regimes, *Bull. Seismol. Soc. Am.* **89**, 1156–1170.

Bureau of Reclamation
P.O. Box 25007 86-68330
Denver, Colorado 80225
(D.R.H.O.)

Department of Earth Science
University of California, Santa Barbara
Santa Barbara, California 93106
sma@crustal.ucsb.edu
(S.M.)

Department of Earth Science and Institute for Crustal Studies
University of California, Santa Barbara
Santa Barbara, California 93106
ralph@crustal.ucsb.edu
(R.J.A.)